The negatively charged carboxy-terminal tail of β-tubulin promotes proper chromosome segregation

Colby P. Fees[a], Jayne Aiken[a], Eileen T. O'Toole[b], Thomas H. Giddings, Jr.[c], and Jeffrey K. Moore[a,*]
[a]Department of Cell and Developmental Biology, University of Colorado School of Medicine, Aurora, CO 80045;
[b]Boulder Laboratory for 3D Electron Microscopy of Cells and [c]Department of Molecular, Cellular, and Developmental Biology, University of Colorado Boulder, Boulder, CO 80309

ABSTRACT **Despite the broadly conserved role of microtubules in chromosome segregation, we have a limited understanding of how molecular features of tubulin proteins contribute to the underlying mechanisms. Here we investigate the negatively charged carboxy-terminal tail domains (CTTs) of α- and β-tubulins, using a series of mutants that alter or ablate CTTs in budding yeast. We find that ablating β-CTT causes elevated rates of chromosome loss and cell cycle delay. Complementary live-cell imaging and electron tomography show that β-CTT is necessary to properly position kinetochores and organize microtubules within the assembling spindle. We identify a minimal region of negatively charged amino acids that is necessary and sufficient for proper chromosome segregation and provide evidence that this function may be conserved across species. Our results provide the first in vivo evidence of a specific role for tubulin CTTs in chromosome segregation. We propose that β-CTT promotes the ordered segregation of chromosomes by stabilizing the spindle and contributing to forces that move chromosomes toward the spindle poles.**

Monitoring Editor
Kerry S. Bloom
University of North Carolina

Received: May 20, 2015
Revised: Mar 30, 2016
Accepted: Mar 30, 2016

INTRODUCTION

During mitosis, sister chromatids are separated through a sequence of events orchestrated by a bipolar network of dynamic microtubules known as the mitotic spindle. The spindle assembles from two microtubule nucleation hubs, the spindle poles, which surround the duplicated genome. Microtubules growing out from the spindle poles sample space through cycles of assembly and disassembly until they form linkages that stabilize the spindle and attach to chromatids. The spindle is stabilized by interpolar microtubules (iMTs), a class of microtubules from opposite poles that align in an antiparallel manner, forming extensive lateral contacts. Chromatids attach to kinetochore microtubules (kMTs), a class of microtubules that bind to kinetochores (KTs), multiprotein complexes that assemble at centromeric regions of DNA. These classes of spindle microtubules play unique and important roles that guide chromatid separation.

Sister chromatids must first become bioriented, with the KTs of each sister attaching to kMTs emanating from opposite spindle poles. The progress of biorientation is monitored by signaling pathways that respond to aberrant attachment. Unattached KTs are detected by the spindle assembly checkpoint (SAC), which blocks progression into anaphase (Foley and Kapoor, 2013; Etemad *et al.*, 2015; Tauchman *et al.*, 2015). Syntelic attachments, which arise when both sister chromatids attach to microtubules emanating from the same spindle pole, fail to generate tension and are disrupted by the aurora B/ Ipl1 kinase (Lampson and Cheeseman, 2011).

The positions of bioriented sister chromatids are controlled by a balance of forces within the spindle. The strongest evidence for this force balance model comes from studies in budding yeast, which features a relatively simple and well-defined spindle (Winey and Bloom, 2012). Spindle microtubules generate outwardly directed forces that pull each sister toward opposite spindle poles. Major contributors to outward forces include the microtubule motors kinesin-14 and kinesin-5, which organize and generate forces on iMTs, respectively, to push the spindle poles apart (Saunders and Hoyt, 1992; Saunders *et al.*, 1997; Hepperla *et al.*, 2014). Outward forces are opposed by inwardly directed forces that hold sister chromatids

This article was published online ahead of print in MBoC in Press (http://www.molbiolcell.org/cgi/doi/10.1091/mbc.E15-05-0300) on April 6, 2016.

*Address correspondence to: Jeff Moore (jeffrey.moore@ucdenver.edu).

Abbreviations used: CENIV, centromere of chromosome IV; CTT, carboxy-terminal tail; iMT, interpolar microtubule; kMT, kinetochore microtubule; KT, kinetochore; SAC, spindle assembly checkpoint; SPB, spindle pole body; WT, wild type.

together. Major contributors to inward forces include loops of pericentric chromatin that are bound together by cohesin (Bouck and Bloom, 2007; Stephens *et al.*, 2013; Chacon *et al.*, 2014). This balance of forces sets the size of the spindle and prepares sister chromatids to separate and move to the spindle poles at anaphase.

How are spindle microtubules regulated to support these various roles? The best-studied role for spindle microtubules is in KT attachment. KTs attach to microtubules through multiple binding modules. The Ndc80 complex binds microtubules through two modules—calponin homology domains in the Ndc80 and Nuf2 subunits, and an unstructured, positively charged N-terminal tail domain in Ndc80 (Wigge and Kilmartin, 2001; Wei *et al.*, 2007; Ciferri *et al.*, 2008; Alushin *et al.*, 2010; Sundin *et al.*, 2011). The Ndc80 tail enhances binding through electrostatic interaction with the microtubule surface and is critical for regulating attachment. When sisters attach to microtubules from the same spindle pole, the microtubule–KT interface is disrupted by the aurora B/Ipl1 and Msp1 kinases, which phosphorylate the Ndc80 tail, as well as other substrates (DeLuca *et al.*, 2006; Guimaraes *et al.*, 2008; Miller *et al.*, 2008; Kemmler *et al.*, 2009; Alushin *et al.*, 2012; Sarangapani *et al.*, 2013; Zaytsev *et al.*, 2015). In budding yeast, the role of the Ndc80 tail appears to overlap with the Dam1 complex, which interacts with and recruits the Ndc80 complex to microtubule plus ends (Lampert *et al.*, 2010). Like Ndc80, Dam1 binds to microtubules through electrostatic interactions, and it is targeted for phosphorylation by aurora B/Ipl1 and Mps1 (Cheeseman *et al.*, 2002; Westermann *et al.*, 2005; Shimogawa *et al.*, 2006). Mutants impairing either Ndc80's tail or Dam1 partially disrupt chromosome segregation, but combining these mutations produces severe defects (Demirel *et al.*, 2012; Lampert *et al.*, 2013; Kalantzaki *et al.*, 2015). The complexity of the microtubule–KT interactions underscores the importance of the regulatory mechanisms that promote proper attachment.

In contrast to the KTs, a mechanistic understanding of how microtubules contribute to this highly regulated process is lacking. Tubulin proteins exhibit molecular diversity in genetically encoded amino acid sequences, as well as posttranslational modifications. Nearly all of this diversity is found in the negatively charged carboxy-terminal tail (CTT) regions of α- and β-tubulin, which decorate the surface of microtubules (Roll-Mecak, 2015). CTTs are known to support electrostatic interactions with KTs. For example, biochemically removing CTTs disrupts binding to Ndc80 and Dam1 in vitro (Westermann *et al.*, 2005; Ciferri *et al.*, 2008). However, the roles of CTTs in a complex cellular environment are undefined. In this study, we use mutants that alter or ablate CTTs of α- and β-tubulin in budding yeast to test the role of CTTs in vivo and gain new insight into chromosome segregation mechanisms. Our results demonstrate a specific role for the CTT of β-tubulin in promoting the fidelity of chromosome segregation and timely cell cycle progression. Mutant cells lacking β-CTT exhibit defects in KT positioning and disorganized spindle microtubules. We identify a short region of negatively charged amino acid residues in β-CTT that are necessary and sufficient for high-fidelity chromosome segregation and provide evidence that the role of β-CTT is conserved across species.

RESULTS

β-CTT promotes proper chromosome segregation

We first tested whether CTTs of α- or β-tubulin are important for chromosome segregation by measuring the loss of a nonessential chromosome fragment (Figure 1A; Spencer *et al.*, 1990). Mutants lacking β-CTT (*tub2*-430Δ) exhibit a fivefold increase in chromosome loss events compared with wild type (WT; Figure 1B). In contrast, mutants either lacking the major α-CTT (*tub1*-442Δ) or all α-CTTs

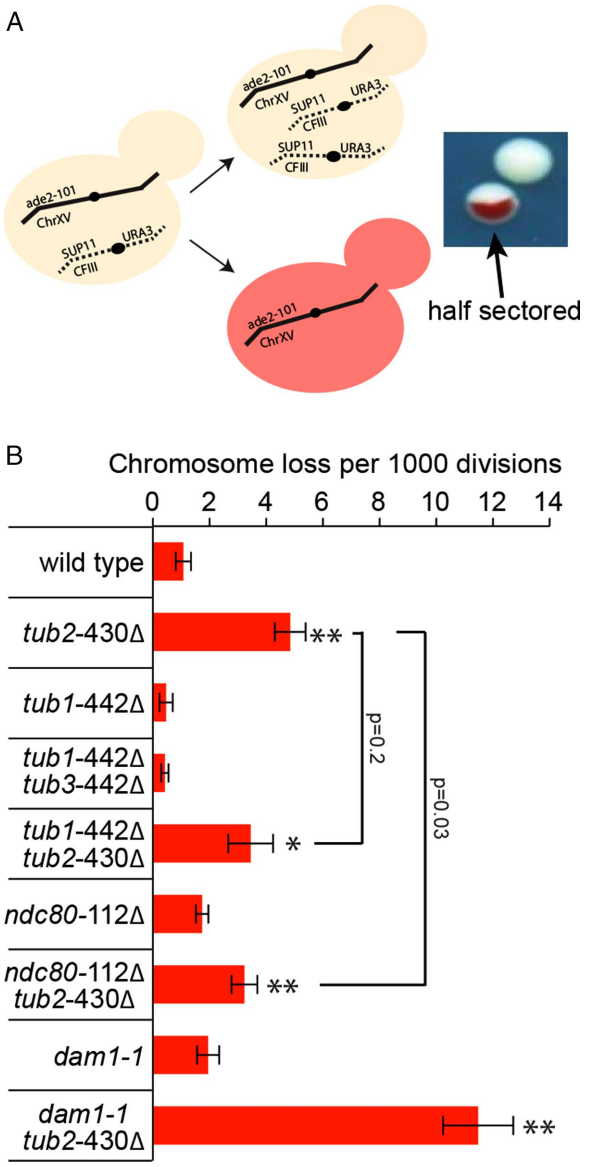

FIGURE 1: β-CTT is important for chromosome segregation. (A) Schematic of chromosome loss assay. (B) Chromosome loss frequency per 1000 divisions. Values are based on the total number of half-sectored colonies divided by the total number of colonies analyzed from at least three separate experiments. Error bars are SE of proportion. *$p = 0.01$, **$p < 0.0001$, determined by chi-square text with Yates' correction. WT, $n = 14{,}866$; tub2-430Δ, $n = 16{,}299$; tub1-442Δ, $n = 8561$; tub1-442Δ tub2-430Δ, $n = 5504$; ndc80-112Δ, $n = 35{,}662$; ndc80-112Δ tub2-430Δ, $n = 15{,}479$; dam1-1, $n = 12816$; and dam1-1 tub2-430Δ, $n = 7405$.

(*tub1*-442Δ *tub3*-442Δ) are indistinguishable from WT in this assay. Mutants lacking both α-CTT and β-CTT exhibit a rate of chromosome loss that is similar to mutants lacking β-CTT alone (Figure 1B). Therefore β-CTT specifically promotes chromosome segregation.

To examine whether β-CTT might function in a common pathway with KT protein complexes, we used the chromosome loss assay to test for genetic interactions. Yeast mutants that disrupt the Ndc80 tail perturb chromosome segregation and exhibit additive effects when combined with Dam1 mutants (Kemmler *et al.*, 2009; Demirel *et al.*, 2012; Kalantzaki *et al.*, 2015). We found that double mutants combining Ndc80 tail truncation (*ndc80*-112Δ) with β-CTT

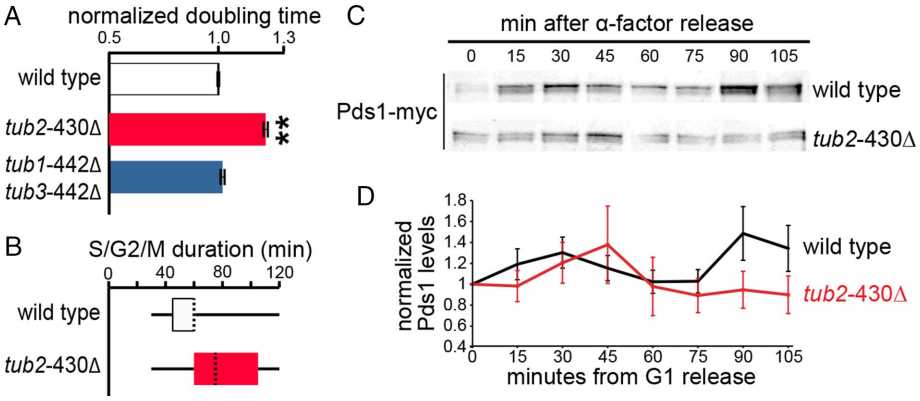

FIGURE 2: β-CTT promotes normal cell cycle progression. (A) Normalized doubling times for WT and CTT mutant cells. Values are the mean from at least four separate experiments. Error bars are SEM. $^{**}p < 0.0001$ determined by *t* test. (B) Duration of S/G2/M determined by measuring the time from bud emergence to separation in cells released from START. Dashed lines are the medians. WT, $n = 617$; tub2-430Δ, $n = 561$. (C) Time course of Pds1/securin levels in synchronized cells released from START. Cells expressing Pds1-13myc were collected at 15- min intervals, prepared for Western blots, and probed with myc antibodies. (D) Pds1-13myc signal at each time point normalized to $t = 0$. Values are averages from three experiments. Error bars are SEM.

truncation lost chromosomes at a rate similar to β-CTT single mutants but greater than *ndc80*-112Δ single mutants (Figure 1B). In contrast, double mutants combining Dam1 impairment (*dam1-1*, at a semipermissive temperature of 25°C) with β-CTT truncation lose chromosomes at a significantly higher rate than either single mutant (Figure 1B). This additive effect is reminiscent of the genetic interaction between *ndc80*-112Δ and *dam1-1* and indicates that cells depend on the function of both β-CTT and the N-terminal tail of Ndc80 when Dam1 is impaired.

β-CTT is necessary for timely progression through mitosis

If chromosome loss in mutants lacking β-CTT arises from defects in spindle assembly, then these mutants might exhibit a SAC-dependent delay in cell cycle progression. We performed a series of experiments to test this prediction. First, we used liquid growth assays to show that mutants lacking β-CTT exhibit a 20% increase in doubling time compared with WT controls and mutants lacking all α-CTTs (*tub1*-442Δ *tub3*-442Δ; Figure 2A). Second, we examined individual synchronized cells, measuring the time from bud emergence (beginning of S phase) to separation (end of mitosis) by time-lapse differential interference contrast microscopy. We found that the duration of S/G2/M is longer and more variable in mutants lacking β-CTT than in WT controls (Figure 2B). Furthermore, 17% of β-CTT mutants remained as large-budded cells at the end of our 135-min experiment, compared with <1% of WT cells. Finally, to specifically measure anaphase, we monitored the kinetics of Pds1/securin degradation in synchronized cells. In WT cells, Pds1/securin levels increase during S phase (15–30 min), decrease at anaphase onset, and rebound when cells enter the next S phase (90 min; Figure 2, C and D; Cohen-Fix *et al.*, 1996). In mutants lacking β-CTT, the decrease in Pds1/securin levels is slower and does not rebound during the course of our experiment (Figure 2, C and D). This suggests that entry into anaphase and the subsequent S phase may be delayed and/or variable in β-CTT mutants. Together with our previous finding that mutants lacking β-CTT depend on SAC activity for viability (Aiken *et al.*, 2014), these results indicate that β-CTT is important for normal progression through mitosis and are consistent with an important role for β-CTT during spindle assembly.

β-CTT promotes KT positioning

We examined KT positioning to determine how β-CTT might contribute to sister chromatid separation. During spindle assembly in yeast, KTs resolve into two clusters as they attach to microtubules emanating from the two spindle pole bodies (SPBs; Goshima and Yanagida, 2000; He *et al.*, 2000; Pearson *et al.*, 2001). We monitored KT position by labeling all KTs with a functional fusion of green fluorescent protein (GFP) to Nuf2. In addition to WT and β-CTT mutants, we also included *dam1-765* mutants in our analysis as a positive control. *dam1-765* is a point mutant in the Dam1 complex that was previously shown to cause KTs to cluster near the spindle poles, away from the spindle center (Shimogawa *et al.*, 2006).

We first compared cells with spindle lengths indicative of metaphase (see *Materials and Methods*). WT cells with metaphase-length spindles consistently exhibit two separated clusters of Nuf2-GFP (Figure 3A and Supplemental Figure S1A). In contrast, β-CTT mutants exhibit variable Nuf2-GFP localization, including single clusters, two WT-like clusters, and two clusters positioned very close to the SPBs (Figure 3B and Supplemental Figure S1B). *dam1-765* mutants consistently exhibit two clusters of Nuf2-GFP very close to the SPBs, as expected (Figure 3C and Supplemental Figure S1C). This initial result suggests that KT position may be more variable in β-CTT mutants.

We used several approaches to quantify differences in Nuf2-GFP localization across populations of preanaphase cells. First, we measured the volume within the cell that is occupied by Nuf2-GFP, based on single–time point confocal *Z*-series imaging. This analysis shows that Nuf2-GFP samples a larger volume within β-CTT mutant cells than in WT controls (Figure 3D). Of importance, total Nuf2-GFP signal per cell is similar in both WT and mutant strains; therefore changes in Nuf2-GFP localization in β-CTT mutants are attributable to changes in position rather than changes in protein levels or number of KTs (Figure 3E). In separate experiments, we found that the localization of an inner KT component, the centromeric histone variant Cse4/CENP-A, is similarly altered in mutants lacking β-CTT (Supplemental Figure S1, D and E).

We next examined Nuf2-GFP localization across different spindle lengths. KTs only resolve into two clusters once the spindle reaches a sufficient length (Marco *et al.*, 2013). In the course of our experiments, we observed that shorter spindles are more abundant in β-CTT mutants (Figure 3F), raising the possibility that differences in Nuf2-GFP localization could be caused by differences in spindle length. To test this possibility, we compared the percentages of cells exhibiting a bilobed distribution of Nuf2-GFP at different spindle lengths. This analysis shows that a similar percentage of WT and β-CTT mutant cells exhibit bilobed Nuf2-GFP, regardless of spindle length (Figure 3G). In contrast, more *dam1-765* mutant cells exhibit bilobed Nuf2-GFP across all spindle lengths examined (Figure 3G). In addition to comparing the separation of KT clusters, we also examined the positions of KT clusters along the spindle axis. In WT spindles shorter than 1100 nm, Nuf2-GFP localizes to a single lobe at the center of the spindle (Figure 3H). In WT spindles longer than 1100 nm, Nuf2-GFP signal shifts away from the spindle center and toward the poles, consistent with a bilobed distribution,

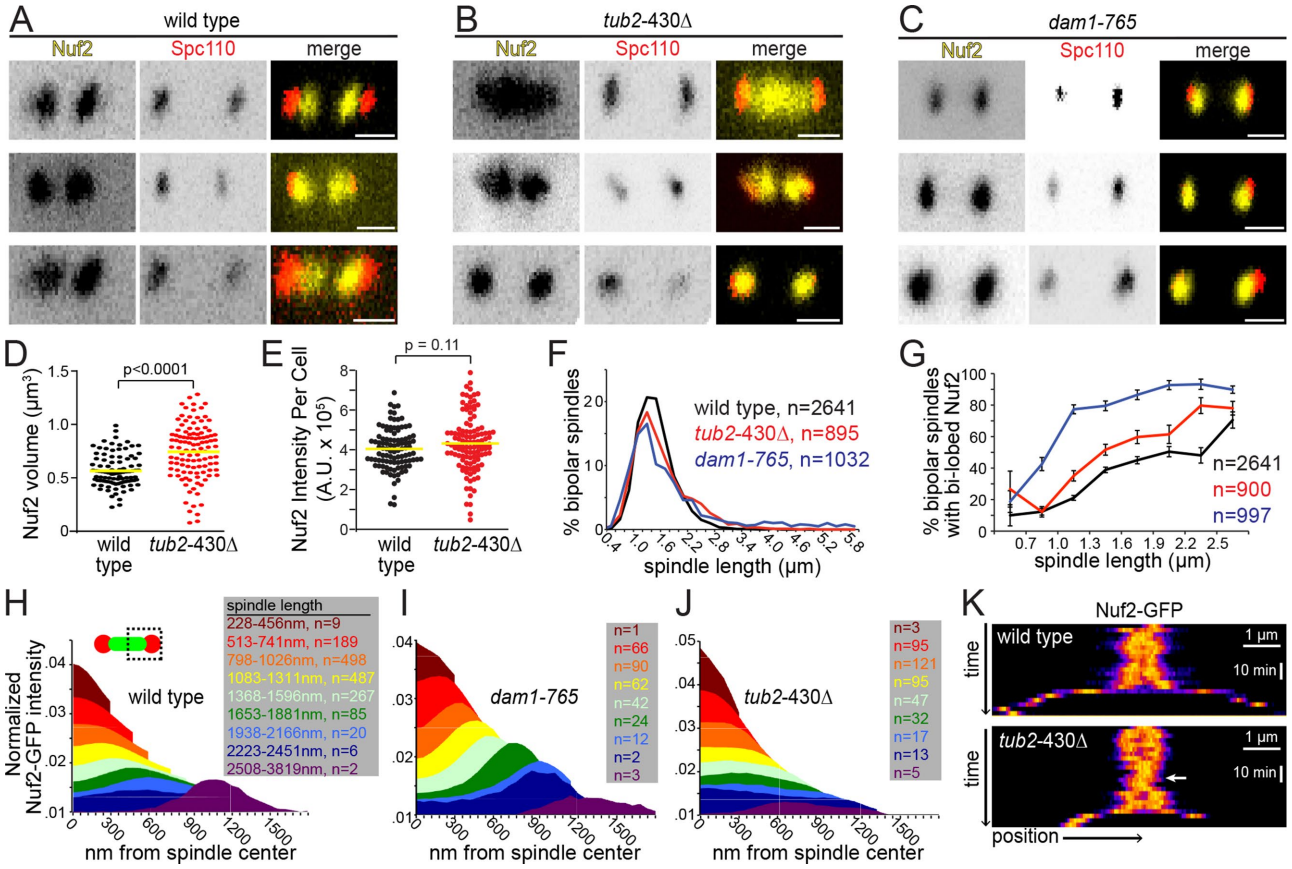

FIGURE 3: β-CTT promotes KT positioning. (A) Maximum intensity projections from 3D confocal images of WT cells expressing Nuf2-GFP and Spc110-DsRed. Scale bars, 1 μm. (B) Maximum intensity projections from 3D confocal images of *tub2*-430Δ cells expressing Nuf2-GFP and Spc110-DsRed. (C) Maximum intensity projections from 3D confocal images of *dam1-765* cells expressing Nuf2-GFP and Spc110-DsRed. (D) Volumetric distribution of Nuf2-GFP signal. Yellow bars denote the mean. The *p* value was determined by *t* test. Strains: WT, $n = 101$; tub2-430Δ, $n = 117$. (E) Sum of intensities of Nuf2-GFP in cells analyzed in three dimensions. (F) Distribution of spindle lengths in asynchronous populations of cells. (G) Proportion of cells exhibiting two peaks of Nuf2-GFP signal as a function of spindle length. Error bars are SE of proportion. (H–J) Distributions of Nuf2-GFP signal measured from the center of the spindle toward the spindle poles and sorted into bins according to spindle lengths. Intensity is internally normalized to the total GFP intensity of each cell. (K) Kymograph of Nuf2-GFP in WT and tub2-430Δ cells. Horizontal lines represent time points at 2.5-min intervals, with pixel values representing the sum of 15 pixels perpendicular to the spindle axis. Arrow shows Nuf2-GFP collapsing into a single lobe in the *tub2*-430Δ cell.

and accumulates further from the spindle center as spindle length increases (Figure 3H and Supplemental Figure S1A). In *dam1-765* mutants, Nuf2-GFP shifts away from the spindle center in spindles as short as 500 nm and becomes strongly concentrated near the poles as spindle length increases (Figure 3I and Supplemental Figure S1C). Our results for WT and *dam1-765* mutant cells are in excellent agreement with previous findings (Shimogawa *et al.*, 2006; Marco *et al.*, 2013). β-CTT mutants do not consistently accumulate Nuf2-GFP near the spindle poles. Although many β-CTT mutant cells exhibit two clusters of Nuf2-GFP, the positions of these clusters in the spindle are highly variable from cell to cell. As a result, the cumulative distributions do not show clear peaks for β-CTT mutant cells, even at longer spindle lengths, which are indicative of metaphase and early anaphase (>1600 nm; Figure 3J). These results suggest that β-CTT is required for maintaining the KT position during spindle assembly and into anaphase.

To further examine the role of β-CTT in maintaining KT position, we used time-lapse microscopy to image Nuf2-GFP in living cells as they transitioned into anaphase. In preanaphase WT control cells, Nuf2-GFP signal gradually resolves into a bilobed distribution until the two lobes rapidly move apart, indicating the onset of anaphase (Figure 3K). In preanaphase β-CTT mutant cells, Nuf2-GFP resolves into a bilobed distribution, but this state is interrupted by prolonged periods of collapse into a single, unresolved lobe (Figure 3K, arrow). At anaphase, the rate of Nuf2-GFP separation in β-CTT mutants is slower than in WT cells; this is consistent with our previous finding that the rate of spindle elongation is slower in β-CTT mutants (Aiken *et al.*, 2014). These results support our conclusion that β-CTT is necessary to maintain KT position in the spindle.

β-CTT is necessary to align KTs with the spindle axis

To identify the cause of KT positioning defects, we imaged a single pair of sister KTs by labeling chromosome IV with GFP inserted 2 kb from the centromere (CENIV). Imaging CENIV sisters clearly reveals the bioriented state—GFP-labeled CENIV resolves into two foci only when attached to kMTs from opposite spindle poles (Figure 4, A and B, and Supplemental Figure S2, A and B; Pearson *et al.*, 2004). Surprisingly, we found that a greater percentage of

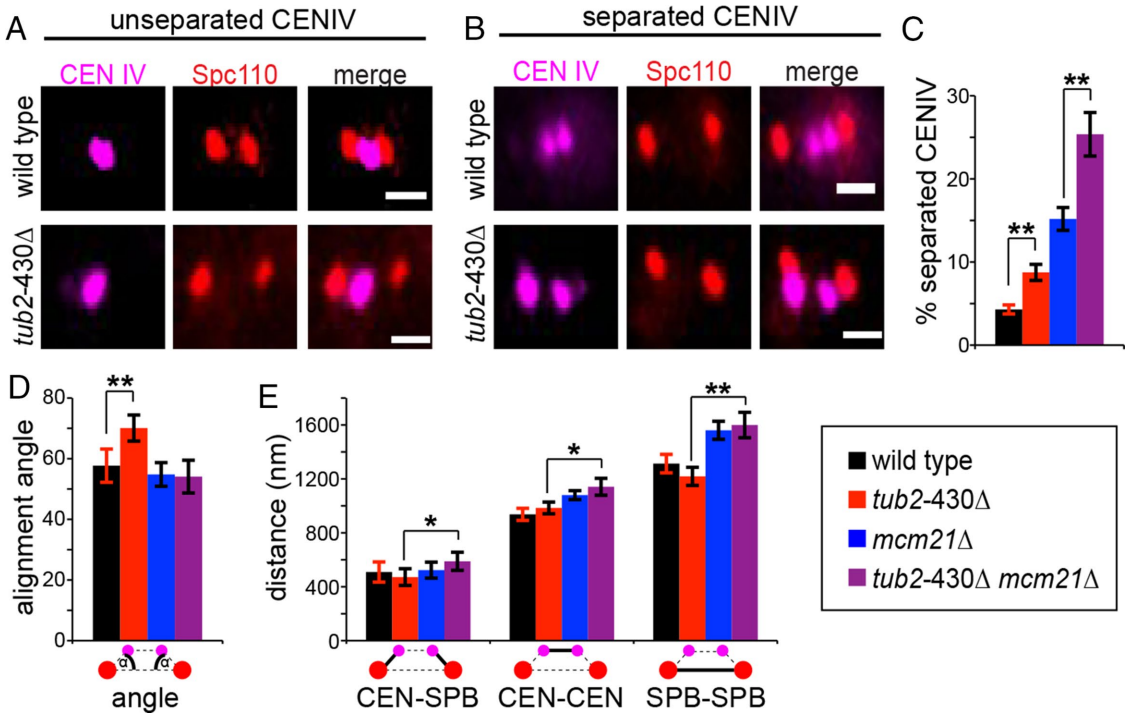

FIGURE 4: Positioning bioriented sister centromeres. (A) Maximum intensity projections from 3D confocal images of WT and *tub2*-430Δ cells expressing CENIV-GFP and Spc110-tdTomato. Scale bars, 1 μm. Preanaphase cells containing a single focus of CENIV-GFP were classified as unseparated. (B) Preanaphase cells containing two foci of CENIV-GFP were classified as separated. (C) Percentage of preanaphase cells exhibiting separated CENIV. $^{**}p < 0.0001$ determined by Fisher's exact test. WT, $n = 1420$; *tub2*-430Δ, $n = 857$; *mcm21*Δ, $n = 685$; and *mcm21*Δ *tub2*-430Δ, $n = 276$. (D) Mean angle between separated CENIV foci and the SPB-SPB axis. Values are mean ± 95% confidence interval (CI). $^{**}p < 0.0001$ determined by *t* test. WT, $n = 61$ cells; *tub2*-430Δ, $n = 109$; *mcm21*Δ, $n = 131$; and *mcm21*Δ *tub2*-430Δ, $n = 70$. (E) Mean distances between CENIV foci and the proximal SPBs, between separated CENIV foci, and between SPBs. Values are mean ±95% CI. $^{*}p < 0.01$, $^{**}p < 0.0001$, determined by *t* test.

preanaphase β-CTT mutant cells exhibit bioriented CENIV compared with preanaphase WT cells (Figure 4C). It is important to note that our method did not resolve CENIV foci separated by <470 nm; therefore the "unseparated" population may include sisters that are bioriented but closely apposed. Nevertheless, β-CTT is clearly not necessary for biorientation.

We next used our CENIV imaging assay to compare the positions of bioriented sister centromeres in the three-dimensional (3D) space of the spindle. To determine whether centromeres are displaced further from the SPB-SPB axis, we calculated the alignment angles of each CENIV sister relative to the SPB-SPB axis (see *Materials and Methods*). These angles are significantly increased in β-CTT mutants compared with WT controls (70 ± 2° [mean ± SEM] in *tub2*-430Δ vs. 58 ± 3° for WT; Figure 4D and Supplemental Figure S2C). kMT lengths, that is, the distances between each CENIV and the nearest SPB, are similar in β-CTT mutants and WT controls, as are the distances between CENIV sisters (Figure 4E and Supplemental Figure S2, D and E). Spindle lengths are slightly shorter in β-CTT mutants ($p = 0.06$; Figures 3F and 4E and Supplemental Figure S2F). These data suggest that β-CTT may normally act to confine bioriented sister centromeres near the SPB-SPB axis.

The positions of bioriented sister centromeres are determined by a balance of outward forces that pull them apart (tensile attachments to kMTs and forces from iMTs on the SPBs) and inward forces hold them together (cohesin, condensin; Bouck and Bloom, 2007; Gardner *et al.*, 2008; Stephens *et al.*, 2013; Chacon *et al.*, 2014). To determine how β-CTT contributes to forces in the spindle, we combined the β-CTT truncation mutation with cohesin mutations that relax inward forces. Disrupting pericentric cohesin with an *mcm21*Δ null mutation increases the percentage of preanaphase cells with bioriented CENIV, increases the distance between sister centromeres, and increases spindle length (Figure 4, C and E; Stephens *et al.*, 2011). We reasoned that if centromere-positioning defects in β-CTT mutants are primarily caused by weaker outward forces, then simultaneously relaxing inward forces with *mcm21*Δ might rescue these defects and lead to intermediate phenotypes. We found that although double mutants combining *tub2*-430Δ with *mcm21*Δ do rescue CENIV alignment angles, spindle lengths are increased similarly to those in *mcm21*Δ single mutants (Figure 4, D and E). In addition, double mutants exhibit significant increases in kMT length and distance between CENIV sisters and a greater percentage of cells with separated CENIV than either single mutant alone (Figure 4, C and E). Therefore disrupting cohesin appears to exacerbate some spindle defects in β-CTT mutants.

β-CTT regulates microtubule organization during spindle assembly

To examine how changes in microtubules might accompany changes in KT position, we mapped the organization and lengths of spindle microtubules using electron tomography. We first compared microtubules in preanaphase spindles, which we identified based on spindle length. Preanaphase WT cells exhibit ~32 short microtubules (<600 nm) and ~8 longer microtubules (>800 nm; Figure 5, A and B). These correspond to kMTs that attach to each KT and iMTs

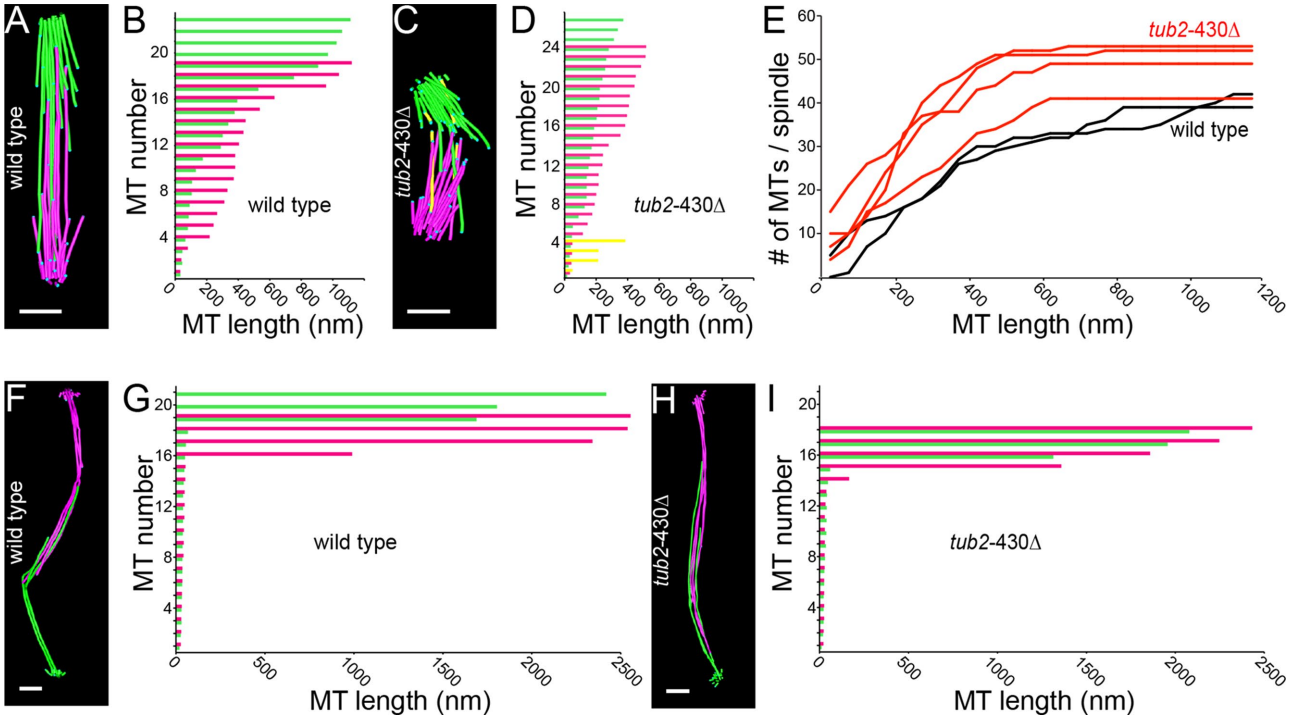

FIGURE 5: β-CTT regulates microtubule length and organization during spindle assembly. (A) Model of spindle microtubules based on a tomographic volume of a preanaphase WT cell. Green lines represent microtubules from one SPB, and pink lines represent microtubules from the other SPB. Scale bars, 200 nm. (B) Histogram of microtubule lengths in the WT cell modeled in A. (C) Model of spindle microtubules based on a tomographic volume of a preanaphase *tub2*-430Δ cell. Yellow lines represent microtubule fragments. (D) Histogram of microtubule lengths in the *tub2*-430Δ cell modeled in C. (E) Histograms of all microtubule lengths from two WT preanaphase spindles (black, $n = 81$ microtubules) and 4 *tub2*-430Δ preanaphase spindles (red, $n = 195$ microtubules). (F) Model of spindle microtubules based on a tomographic volume of an anaphase WT cell. (G) Histogram of microtubule lengths in the WT cell modeled in F. (H) Model of spindle microtubules based on a tomographic volume of an anaphase *tub2*-430Δ cell. (I) Histogram of microtubule lengths in the *tub2*-430Δ cell modeled in H.

that interdigitate to form antiparallel overlaps that stabilize the bipolar spindle, respectively (Winey *et al.*, 1995). Preanaphase spindles in β-CTT mutants differ from WT controls in several respects. First, the distance between SPBs is decreased (Supplemental Figure S3). This is consistent with our light microscopy results and our previous findings from time-lapse imaging (Figure 3F; Aiken *et al.*, 2014).

Second, the two spindle halves are often misaligned and exhibit few interdigitating microtubules (Figure 5C and Supplemental Figure S3). This is reminiscent of an early stage of spindle assembly, before the bipolar state is stabilized (Winey and O'Toole, 2001). Three of four tomograms of preanaphase β-CTT mutant spindles exhibit a clear misalignment of spindle halves, and therefore it is unlikely that this represents a transient intermediate. Instead, β-CTT mutants may linger in this state.

Third, β-CTT mutant spindles contain more microtubules and exhibit differences in microtubule lengths. In general, β-CTT mutant spindles contain a greater frequency of shorter (<200 nm) microtubules and fewer longer microtubules (Figure 5E). Many of these microtubules deviate far from the SPB-SPB axis (Figure 5C and Supplemental Figure S3). The changes in microtubule length and alignment in β-CTT mutants may explain changes in KT position that we observed by light microscopy, including aberrant Nuf2-GFP distribution and deviation of KTs from the SPB-SPB axis (Figures 3 and 4).

Fourth, β-CTT mutant spindles contain microtubule "fragments" that are not connected to SPBs and exhibit flared morphology at both ends (Figure 5C and Supplemental Figure S3, colored yellow). Fragments vary in length and number per cell, as do their location in the spindle. We did not find microtubule fragments in WT cells, and, to our knowledge, they have not been previously reported.

Although β-CTT mutants exhibit microtubule defects in preanaphase spindles, we did not observe defects in anaphase spindles. Anaphase cells for both WT and the β-CTT mutant exhibit ~16 very short (<100 nm) microtubules from each SPB, along with a small number of much longer microtubules that overlap in the center of the spindle (Figure 5, F–I, and Supplemental Figure S3). These represent kMTs and iMTs, respectively. The lengths and number of these microtubules are not significantly different between mutant and WT. We conclude that β-CTT is important for regulating microtubule organization during spindle assembly.

Mapping the region of β-CTT that is important for chromosome segregation

Finally, we sought to gain insight into the mechanism of β-CTT function by mapping the amino acids that are important for its role in chromosome segregation. Yeast β-tubulin is enriched for negatively charged amino acids at residues 431–438 (Figure 6A). We term this region the "acidic patch." Restoring these eight amino acids rescues the defects of *tub2*-430Δ, including chromosome segregation, growth rate, and viability in the absence of SAC activity (Figure 6, B and C; unpublished data). Restoring the acidic patch and the next seven residues (*tub2*-445Δ) also rescues the defects of *tub2*-430Δ (Figure 6, B and C). These results indicate

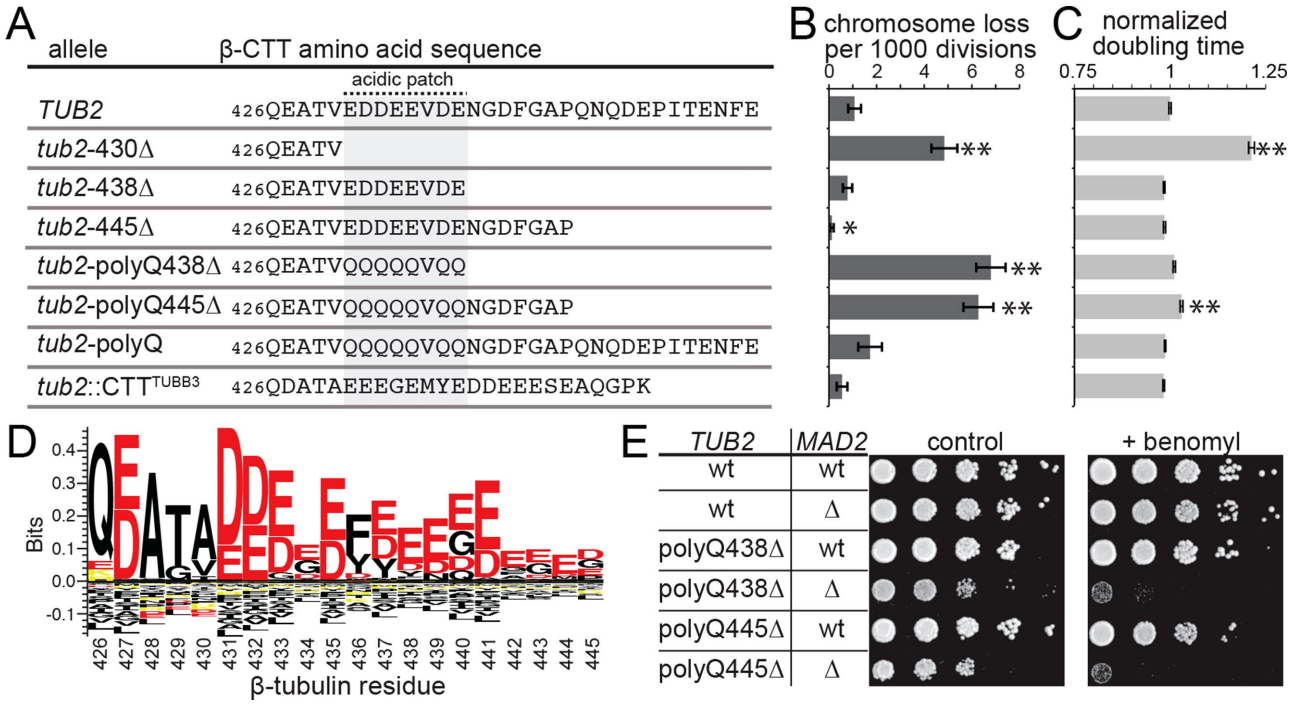

FIGURE 6: Mapping the region of β-CTT that is important for chromosome segregation. (A) Amino acid sequence alignment of WT and mutant β-CTT. The acidic patch is shaded gray. (B) Chromosome loss frequency per 1000 divisions. *p = 0.0001 and **p < 0.0001 determined by chi-square test with Yates' correction. WT, n = 14,866; *tub2*-430Δ, n = 16,299; *tub2*-438Δ, n = 20,492; *tub2*-445Δ, n = 23,932; *tub2*-polyQ438Δ, n = 17,792; *tub2*-polyQ445Δ, n = 15,776; *tub2*-polyQ, n = 6946; and tub2::CTT^{TUBB3}, n = 15,607. (C) Normalized doubling times. (D) Sequence logo for β-tubulin residues 426–445, created from amino acid sequences from 24 β-tubulins (Supplemental Table S1). (E) Genetic interactions with SAC mutants. Tenfold dilution series of strains indicated at left were spotted to rich medium or rich medium supplemented with 10 μg/ml benomyl and grown at 30°C.

that the acidic patch is sufficient for β-CTT function in chromosome segregation.

Although the sequence of the acidic patch is not strictly conserved across β-tubulin isotypes, the enrichment of negatively charged residues is a common feature (Figure 6D and Supplemental Table S1). To determine whether negative charge is necessary for function, we replaced glutamate and aspartate residues in β-CTT with glutamines. Neutralizing these residues in *tub2*-438Δ and *tub2*-445Δ truncation mutants causes levels of chromosome loss that are equivalent to those from complete removal of β-CTT and slightly increases doubling time (Figure 6, A–C). Both of these alleles are viable in combination with mutants that ablate the SAC (*mad2*Δ); however, double mutants are sensitive to a low dose (10 μg/ml) of the microtubule- destabilizing drug benomyl (Figure 6E). Neutralizing acidic patch residues in the context of full-length β-CTT (*tub2*-polyQ) causes mild phenotypes, slightly increasing chromosome loss but with no effect on growth or synthetic effects with SAC mutants (Figure 6, A–D). The charge of the acidic patch is therefore necessary in the context of truncated β-CTT; however, the remaining acidic residues in β-CTT may provide some compensation in the context of full-length β-CTT.

To test whether chromosome segregation is sensitive to sequence differences across β-tubulin isotypes, we replaced the native yeast β-CTT with the CTT from the human βIII isotype TUBB3 (Figure 6A). This *tub2*::CTT^{TUBB3} chimera fully rescues β-CTT function in chromosome segregation and growth rate and is viable in the absence of SAC activity (Figure 6, B and C; unpublished data). Therefore chromosome segregation is highly sensitive to the negative charge of β-CTT but less sensitive to specific amino acid sequence.

DISCUSSION

Our study provides the first in vivo evidence of tubulin's contribution to the electrostatic interactions that regulate the mitotic spindle. We demonstrate that negatively charged amino acid residues within the CTT region of β-tubulin promote proper chromosome segregation. Ablating these residues or neutralizing the charges of their side chains increases chromosome segregation errors and makes cells reliant on the SAC for viability. We propose that the principal role of β-CTT is to organize spindle microtubules to stabilize the spindle and promote the ordered separation of sister chromatids.

The role of β-CTT in spindle assembly is supported by our findings, as well as previous studies. Time-course experiments with synchronized cells show that mutants lacking β-CTT delay the formation of bipolar spindles (Aiken *et al.*, 2014). In the present study, we find that preanaphase spindles are shorter in β-CTT mutants, based on distributions of spindle lengths in asynchronous populations of cells (Figure 3F) and specifically in metaphase cells with bioriented CENIV (Figure 4E). These new results, combined with our previous findings, indicate that β-CTT may contribute to both the early stages of spindle assembly and the subsequent maintenance of spindle stability in metaphase. Our tomographic analyses provide insight into the specific role of β-CTT in these contexts. In contrast to wild-type controls, β-CTT mutants show misalignment of the two halves of the preanaphase spindle and a concomitant lack of interdigitating iMTs (Figure 5 and Supplemental Figure S3). We analyzed four β-CTT

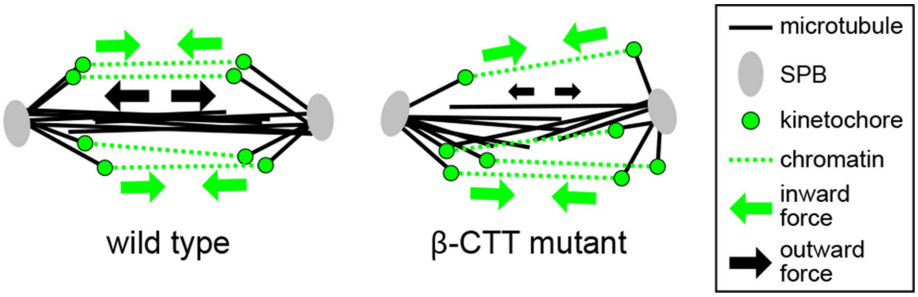

FIGURE 7: Model of spindle organization in wild-type cells and β-CTT mutants. Spindle microtubules (black lines) emanate from SPBs (gray) to form antiparallel overlaps in the spindle center and attach to KTs (green). KT position is determined by a balance of outward forces (black arrows) generated by iMTs and inward forces (green arrows) generated by chromatin (green dashed lines). β-CTT mutants are defective for spindle stability and therefore predicted to generate weaker outward forces. This imbalance shortens the spindle and disrupts KT position.

mutant cells with preanaphase spindles (determined by the distance between SPBs and the lengths of kMTs), and all four exhibit these defects. These characteristics are reminiscent of WT cells during the early stages of spindle assembly and suggest that β-CTT may be necessary for either efficient transit through early stages of spindle assembly or the stabilization of the metaphase spindle (Winey and O'Toole, 2001). Moreover, the kMTs in the mutant cells appear to be grossly disorganized (Figure 5C). The disorganization of kMTs is consistent with the disorganization we observed at the levels of kinetochores and sister centromeres (Figures 3 and 4). Of importance, structural defects in β-CTT mutants are specific to preanaphase spindles; we did not observe similar defects in tomograms of anaphase spindles (Figure 5 and Supplemental Figure S3). Determining the molecular mechanism of β-CTT function during spindle assembly will require further study; however, we speculate that this mechanism may involve electrostatic interactions with positively charged microtubule-binding proteins that promote the alignment and/or cross-linking of interdigitating iMTs.

How could microtubule disorganization lead to defective KT positioning and, ultimately, chromosome missegregation? Our results suggest that β-CTT is not necessary to biorient individual sister KTs but is necessary to cluster KTs near the SPBs and maintain the alignment of KTs along the SPB-SPB axis (Figures 3 and 4). Of importance, the defects we observe in β-CTT mutants are quite different from those observed in mutants that alter KT-microtubule binding (e.g., *dam1-765*; Figure 3I; Shimogawa *et al.*, 2006) or inhibit biorientation (e.g., *ipl1* or *stu2* mutants; Marco *et al.*, 2013). We propose that β-CTT may contribute to both the generation of outward forces on KTs and the maintenance of kMTs along the spindle axis (Figure 7). Our analysis of *tub2*-430Δ *mcm21*Δ double mutants supports this model. If the spindle defects in β-CTT mutants were attributable to weakened outward forces alone, then simultaneously weakening inward forces with the cohesin mutant would be expected to restore the balance of forces in the spindle, and double mutants should therefore exhibit intermediate phenotypes relative to either single mutant alone. This relationship was demonstrated for mutants that disrupt kinesin-5 motors (Bouck and Bloom, 2007). We do find that *tub2*-430Δ *mcm21*Δ double mutants rescue KT alignment along the SPB-SPB axis, indicating that imbalanced spindle forces contribute to KT positioning defects (Figure 4D). However, *tub2*-430Δ *mcm21*Δ double mutants also exhibit longer spindles that are similar to those in *mcm21*Δ single mutants (Figure 4E) and an even greater percentage of cells with separated CENIV than for either single mutant (Figure 4C). Therefore loss of the cohesin network (*mcm21*Δ) is synergistic with loss of β-CTT mutants, indicating that β-CTT also has an important role in clustering centromeres along the spindle axis. Taken together, these results show that whereas outward forces are affected in β-CTT mutants, the mechanism could also involve defective kinetochore microtubule organization. Another question that arises is whether the distortions of spindle structure in β-CTT mutants alter normal functions like the surveillance of KT attachment by the SAC. This could reconcile the paradox of how β-CTT mutants experience cell cycle delay and chromosome segregation errors despite the apparent efficiency of biorientation.

An alternative but not mutually exclusive model is that β-CTT could regulate electrostatic interactions at the KT–microtubule interface. We find no evidence of deficient biorientation in β-CTT mutants, indicating that interactions with tubulin CTTs are not necessary for KTs to attach to microtubules in budding yeast. This result highlights molecular differences between the yeast and mammalian systems, in which electrostatic interactions play an important role in regulating KT attachment (DeLuca *et al.*, 2006; Guimaraes *et al.*, 2008). One possible explanation for these differences is that yeast possess other unique modes for binding KTs to microtubules, such as the Dam1 complex, which might act in parallel to electrostatic interactions with tubulin CTTs. Consistent with this, our epistasis experiments in Figure 1B reveal strongly additive chromosome segregation defects in double mutants that simultaneously ablate β-CTT and impair the Dam1 complex. Therefore fully functional Dam1 appears to become necessary for chromosome segregation when β-CTT is missing, consistent with the two acting in parallel. Previous studies of yeast mutants that lack the N-terminal tail of Ndc80 found a similar relationship with the Dam1 complex (Demirel *et al.*, 2012). Collectively, these results support a model in which the Ndc80 tail and β-CTT act together to support a KT–microtubule interface that acts in parallel to the Dam1 complex.

Finally, our findings raise the question of whether molecular changes at the level of β-CTT, either genetically encoded or posttranslational, may provide a mechanism for regulating mitotic spindle function. CTT sequences are highly divergent across species and across tubulin isotypes within a species (Supplemental Table S1). Furthermore, CTTs are major targets of posttranslational modifications that dramatically alter CTT structure and charge (Roll-Mecak, 2015). Together these differences create a highly variable molecular landscape at the microtubule surface. Our results indicate that sequence differences between β-tubulin isotypes do not alter spindle function as long as the CTT region contains a sufficient quorum of negatively charged amino acid residues (Figure 6). Whether posttranslational modifications of β-CTT alter spindle function remains an open and important question.

MATERIALS AND METHODS

Chemicals and reagents were from Fisher Scientific (Pittsburgh, PA) and Sigma-Aldrich (St. Louis, MO), unless stated otherwise.

Yeast strains and manipulation

General yeast manipulation, media, and transformation were performed by standard methods (Amberg *et al.*, 2005). A detailed list of strains is provided in Supplemental Table S2. Mutant alleles of

TUB1, *TUB2*, and *TUB3* were generated at the native chromosomal loci as described in Aiken *et al.* (2014). *ndc80*-112Δ, which lacks the N-terminal tail encoded by the first 112 amino acids, was generated by removing codons 2–112 from the native *NDC80* locus. *dam1-1* was generated by creating a C111Y substitution mutation at the native *DAM1* locus, recreating the previously identified *dam1-1* allele (Jones *et al.*, 1999). *dam1-765* was generated by cloning the *dam1-765* allele (a gift from Trisha Davis, University of Washington, Seattle, WA), containing the S221F substitution, into a plasmid containing the *Schizosaccharomyces pombe his5* marker, creating plasmid pJM0283. The *dam1-765::SpHis5* cassette was then amplified by PCR and integrated into the native locus, replacing the native *DAM1* allele. Strains expressing CENIV labeled with GFP were derived from those described in Brito *et al.* (2010). All other fluorescent fusions were integrated at the endogenous chromosomal loci.

Chromosome loss assay

Retention of a nonessential chromosome fragment carrying an ochre-suppressing allele of the *SUP11* tRNA, which suppresses premature termination of *ade2-101* translation, was measured as described in Koshland and Hieter (1987). Cultures were grown overnight at 30°C in synthetic –URA dropout medium. The saturated cultures were diluted 100-fold, and cells were counted using a hemocytometer. Two hundred cells were plated on yeast extract/peptone/dextrose (YPD) and grown for 3-4 d at 30°C before being moved to 4°C for 2 d for color development. The plates were scanned at 600-dpi resolution in 24-bit color. Colonies were counted either by hand or by using a custom-made MATLAB program. The half-red-sectored colonies were divided by the total number of colonies to determine chromosome loss frequency. Each strain was tested in at least three separate experiments, with at least 1000 colonies scored per experiment.

Liquid growth assay

Cells were grown in 3 ml of YPD overnight at 30°C and diluted 50-fold into fresh medium. The diluted cultures were then aliquoted into a 96-well plate, with eight replicates per experiment, and incubated at 30°C with single orbital shaking in a Cytation3 plate reader (BioTek, Winooski, VT). The OD_{600} was measured every 5 min for 24 h. Doubling time was calculated by fitting the growth curves to a nonlinear exponential growth curve (GraphPad Prism version 6.0; GraphPad, San Diego, CA).

Budding duration analysis

Budding duration was determined using time-lapse microscopy of α-factor–synchronized cultures grown to mid log phase (WT, 2 h; tub2-430Δ, 3 h). Cultures were released from arrest by washing twice and resuspending cells in fresh medium supplemented with protease, then mounted on slides and imaged every 15 min for 135 min. Images were collected on a Nikon Ti-E microscope (Nikon, Melville, NY) equipped with a 100×/numerical aperture (NA) 1.49 CFI 60 Apochromat objective, PEKA light engine (Lumencore, Beaverton, OR), and scientific complementary metal-oxide semiconductor camera (ORCA-Flash 4.0 LT; Hamamatsu Photonics, Shizuoka, Japan) using NIS Elements software (Nikon).

Time course of Pds1 levels

Cells were grown to early log phase at 30°C in 100 ml of YPD and arrested with two pulses of α- factor for 90 and 60 min, respectively. The cells were pelleted, washed with water, resuspended into 130 ml of fresh YPD, and returned to the 30°C shaking incubator. We collected 15-ml culture samples at 15-min intervals, which were washed, pelleted, and lysed by bead beating. The total protein concentration of the clarified lysate was determined by Bradford assay, and all samples were normalized. Samples were run on SDS–PAGE, transferred to nitrocellulose membrane, and blocked overnight at 4°C. Membranes were probed with mouse α-myc (MA1-980; 1:1000; Thermo Scientific, Waltham, MA) and goat α–mouse-800 (926-32210; 1:10,000; LI-COR Biosciences, Superior, NE) and imaged on an Odyssey Imager (LI-COR Biosciences). Intensities of Pds1-myc bands were quantified using ImageJ (National Institutes of Health, Bethesda, MD). Pixel intensities were measured across an equivalent area for each Western blot lane within a time course, and the intensities of these regions were divided by the intensity at $t = 0$ to obtain a ratio of each time point to the initial level.

Microscopy and image analysis

Images were collected on a Nikon Ti-E microscope equipped with a 100×/1.45 NA CFI Plan Apo objective, piezoelectric stage (Physik Instrumente, Auburn, MA), spinning-disk confocal scanner unit (CSU10; Yokogawa, Tokyo, Japan), 488- and 561-nm lasers (Agilent Technologies, Santa Clara, CA), and an electron-multiplying charge-coupled device (CCD) camera (iXon Ultra 897; Andor Technology, Belfast, United Kingdom) using NIS Elements software. Cells were grown asynchronously to early log phase in nonfluorescent medium, mounted on a slab of 2% agarose, and sealed beneath a coverslip with Vaseline/lanolin/paraffin at 1:1:1. During acquisition, the temperature of the stage was 25°C. The *Z*-series consisted of 21 images separated by 300 nm.

Preanaphase cells were identified in asynchronous populations based on spindle length, which was determined by measuring the distance between SPBs labeled with Spc110-RFP. The distribution of all spindle lengths from asynchronous cells shows a peak that reflects metaphase spindle length, and the mean values for WT (1.8 μm) and tub2-430Δ (1.6 μm) cells were consistent with the average spindle length just before anaphase onset, which we previously defined using time-lapse imaging (Figure 3F; Aiken *et al.*, 2014). We therefore defined "preanaphase" as bipolar spindles shorter than the mean of the total population.

The volume occupied by Nuf2-GFP was determined from single–time point confocal stacks of cells expressing Nuf2-GFP and Spc110-DsRed from the native loci. Preanaphase cells were identified and segmented from the field using a custom ImageJ macro. After segmentation, a low-bandpass Butterfield filter and semiautomated Otsu intensity thresholding application were used to identify Nuf2-GFP signal and generate a binary mask. Masks were then converted to regions of interest (ROIs) using connected-components pixel labeling. The total number of pixels in the ROI was then converted into micrometers cubed using an empirically derived pixel calibration in *x* and *y* (57 nm/pixel) and a *z*-depth of the stack (300 nm). We validated this approach by comparing the sum of Nuf2-GFP pixel values measured in each cell and found that the data exhibited a normal distribution that was not different between WT and βΔCTT mutant cells.

The distribution of Nuf2-GFP along the spindle axis was measured by using a custom MATLAB program to determine the centroid coordinates of the spindle poles (labeled with Spc110-DsRed). Briefly, image stacks were compressed to a sum intensity projection and then processed using a Laplacian filter and Otsu intensity thresholding to generate binary masks. Two-dimensional ROIs were defined using connected-components pixel labeling, and the *x*,*y*-coordinates of the centroids of these ROIs were calculated using MATLAB. Spindle lengths were calculated between centroids in MATLAB using a distance formula. Each sum intensity projection

image was rotated using calculated angle that aligned the spindle along a horizontal axis. Images were then cropped to 10 pixels (570 nm) on either side of the SPBs and 7 pixels above and below the SPB-SPB axis (800 nm total). Line scans of Nuf2-GFP intensity were then generated by summing pixel values in each 14-pixel column along the SPB-SPB axis.

Centroids of CENIV-GFP and Spc110-RFP were determined by first segmenting individual cells and then using a custom MATLAB program to determine the centroid coordinates. Briefly, image stacks were processed using Laplacian filter and Otsu intensity thresholding to generate binary masks. Three-dimensional ROIs were defined in *z*-stacks using connected-components pixel labeling, and the *x*,*y*,*z*-coordinates of the centers of these ROIs were calculated using MATLAB. kMT lengths were calculated in MATLAB using a 3D distance formula, based on the distances from the centroid of a bioriented sister CENIV and the nearest SPB. kMT angles were calculated using the inverse cosine of kMT length divided by the distance from CENIV to the SPB-SPB axis.

Electron tomography

Cells were prepared for electron microscopy as described in Giddings *et al.* (2001). Briefly, aliquots from log-phase liquid cultures were collected onto a 0.45-µm Millipore filter (EMD Millipore, Billerica, MA) by vacuum filtration. The cells were then frozen using a Wohlwend Compact 02 high-pressure freezer (Wohlwend, Sennwald, Switzerland), freeze substituted in 0.25% glutaraldehyde and 0.1% uranyl acetate in acetone, and embedded in Lowicryl HM20 resin. Serial sections (250 nm) were collected onto Formvar-coated slot grids and poststained with 2% uranyl acetate followed by lead citrate. Colloidal gold particles were affixed to the sections to serve as fiducial markers for alignment.

Tomography was performed essentially as described in O'Toole *et al.* (2002). Dual-axis tilt series were collected using a Tecnai F20 or F30 microscope (FEI, Hillsboro, OR) using the SerialEM program for data acquisition (Mastronarde, 2005). Tilt-series data were acquired from serial sections at a pixel size of 1.2 nm using a Gatan (Pleasanton, CA) CCD camera. Tomographic volumes were computed using the IMOD software package (Kremer *et al.*, 1996; Mastronarde, 1997). Volumes from three to or four serial sections were joined, and the spindle microtubules were modeled using the 3 dmod program of the IMOD software package. Microtubule lengths were computed from the model contour data.

Benomyl sensitivity

Cells were grown in YPD to saturation at 30°C, and a 10-fold dilution series of each was spotted to either YPD or YPD supplemented with 10 µg/ml benomyl. Plates were grown at 30°C for 2 d.

Sequence logo

A probability-weighted Kullback–Leibler sequence logo of β-CTT residues 426–445 was created using the Seq2Logo server (www.cbs.dtu.dk/biotools/Seq2Logo; Thomsen and Nielsen, 2012) based on 24 β-tubulin sequences from diverse species (Supplemental Table S1). Positive bit scores indicate amino acids that are enriched at each position, and negative bit scores indicate amino acids that are depleted. Negatively charged residues are labeled red, and positively charged residues are labeled yellow.

ACKNOWLEDGMENTS

We thank Christopher Lawton and Domenico Galati for helping with data collection and analysis; Christina Clarissa of the MCDB EM Suite for freezing and preparing samples for electron microscopy; the Boulder Laboratory for 3D Electron Microscopy of Cells for use of their equipment; Philip Hieter (University of British Columbia, Vancouver, Canada), Yanchang Wang (Florida State University, Tallahassee, FL), Trisha Davis (University of Washington, Seattle, WA), Kerry Bloom (University of North Carolina at Chapel Hill, Chapel Hill, NC), and Michael McMurray (University of Colorado School of Medicine, Aurora, CO) for sharing reagents and Chad Pearson (University of Colorado School of Medicine) for helpful discussions. This work was supported by National Institutes of Health Grants R00GM092968 and R01GM112893 (to J.K.M.). E.O.T. was supported by Grant P41GM103431 from the National Institute of General Medical Sciences to the Boulder Laboratory for 3D Electron Microscopy of Cells.

REFERENCES

Aiken J, Sept D, Costanzo M, Boone C, Cooper JA, Moore JK (2014). Genome-wide analysis reveals novel and discrete functions for tubulin carboxy-terminal tails. Curr Biol 24, 1295–1303.

Alushin GM, Musinipally V, Matson D, Tooley J, Stukenberg PT, Nogales E (2012). Multimodal microtubule binding by the Ndc80 kinetochore complex. Nat Struct Mol Biol 19, 1161–1167.

Alushin GM, Ramey VH, Pasqualato S, Ball DA, Grigorieff N, Musacchio A, Nogales E (2010). The Ndc80 kinetochore complex forms oligomeric arrays along microtubules. Nature 467, 805–810.

Amberg DC, Burke D, Strathern J (2005). Methods in Yeast Genetics, Cold Spring Harbor, NY: Cold Spring Harbor Laboratory Press.

Bouck DC, Bloom K (2007). Pericentric chromatin is an elastic component of the mitotic spindle. Curr Biol 17, 741–748.

Brito IL, Yu HG, Amon A (2010). Condensins promote coorientation of sister chromatids during meiosis I in budding yeast. Genetics 185, 55–64.

Chacon JM, Mukherjee S, Schuster BM, Clarke DJ, Gardner MK (2014). Pericentromere tension is self-regulated by spindle structure in metaphase. J Cell Biol 205, 313–324.

Cheeseman IM, Anderson S, Jwa M, Green EM, Kang J, Yates JR, Chan CS, Drubin DG, Barnes G (2002). Phospho-regulation of kinetochore-microtubule attachments by the Aurora kinase Ipl1p. Cell 111, 163–172.

Ciferri C, Pasqualato S, Screpanti E, Varetti G, Santaguida S, Dos Reis G, Maiolica A, Polka J, De Luca JG, De Wulf P, *et al.* (2008). Implications for kinetochore-microtubule attachment from the structure of an engineered Ndc80 complex. Cell 133, 427–439.

Cohen-Fix O, Peters JM, Kirschner MW, Koshland D (1996). Anaphase initiation in Saccharomyces cerevisiae is controlled by the APC-dependent degradation of the anaphase inhibitor Pds1p. Genes Dev 10, 3081–3093.

DeLuca JG, Gall WE, Ciferri C, Cimini D, Musacchio A, Salmon ED (2006). Kinetochore microtubule dynamics and attachment stability are regulated by Hec1. Cell 127, 969–982.

Demirel PB, Keyes BE, Chaterjee M, Remington CE, Burke DJ (2012). A redundant function for the N-terminal tail of Ndc80 in kinetochore-microtubule interaction in Saccharomyces cerevisiae. Genetics 192, 753–756.

Etemad B, Kuijt TE, Kops GJ (2015). Kinetochore-microtubule attachment is sufficient to satisfy the human spindle assembly checkpoint. Nat Commun 6, 8987.

Foley EA, Kapoor TM (2013). Microtubule attachment and spindle assembly checkpoint signalling at the kinetochore. Nat Rev Mol Cell Biol 14, 25–37.

Gardner MK, Bouck DC, Paliulis LV, Meehl JB, O'Toole ET, Haase J, Soubry A, Joglekar AP, Winey M, Salmon ED, *et al.* (2008). Chromosome congression by kinesin-5 motor-mediated disassembly of longer kinetochore microtubules. Cell 135, 894–906.

Giddings THJ, O'Toole ET, Morphew M, Mastronarde DN, McIntosh JR, Winey M (2001). Using rapid freeze and freeze-substitution for the preparation of yeast cells for electron microscopy and three-dimensional analysis. Methods Cell Biol 67, 27–42.

Goshima G, Yanagida M (2000). Establishing biorientation occurs with precocious separation of the sister kinetochores, but not the arms, in the early spindle of budding yeast. Cell 100, 619–633.

Guimaraes GJ, Dong Y, McEwen BF, Deluca JG (2008). Kinetochore-microtubule attachment relies on the disordered N-terminal tail domain of Hec1. Curr Biol 18, 1778–1784.

He X, Asthana S, Sorger PK (2000). Transient sister chromatid separation and elastic deformation of chromosomes during mitosis in budding yeast. Cell 101, 763–775.
Hepperla AJ, Willey PT, Coombes CE, Schuster BM, Gerami-Nejad M, McClellan M, Mukherjee S, Fox J, Winey M, Odde DJ, *et al.* (2014). Minus-end-directed kinesin-14 motors align antiparallel microtubules to control metaphase spindle length. Dev Cell 31, 61–72.
Jones MH, Bachant JB, Castillo AR, Giddings THJ, Winey M (1999). Yeast Dam1p is required to maintain spindle integrity during mitosis and interacts with the Mps1p kinase. Mol Biol Cell 10, 2377–2391.
Kalantzaki M, Kitamura E, Zhang T, Mino A, Novak B, Tanaka TU (2015). Kinetochore-microtubule error correction is driven by differentially regulated interaction modes. Nat Cell Biol 17, 421–433.
Kemmler S, Stach M, Knapp M, Ortiz J, Pfannstiel J, Ruppert T, Lechner J (2009). Mimicking Ndc80 phosphorylation triggers spindle assembly checkpoint signalling. EMBO J 28, 1099–1110.
Koshland D, Hieter P (1987). Visual assay for chromosome ploidy. Methods Enzymol 155, 351–372.
Kremer JR, Mastronarde DN, McIntosh JR (1996). Computer visualization of three-dimensional image data using IMOD. J Struct Biol 116, 71–76.
Lampert F, Hornung P, Westermann S (2010). The Dam1 complex confers microtubule plus end-tracking activity to the Ndc80 kinetochore complex. J Cell Biol 189, 641–649.
Lampert F, Mieck C, Alushin GM, Nogales E, Westermann S (2013). Molecular requirements for the formation of a kinetochore-microtubule interface by Dam1 and Ndc80 complexes. J Cell Biol 200, 21–30.
Lampson MA, Cheeseman IM (2011). Sensing centromere tension: Aurora B and the regulation of kinetochore function. Trends Cell Biol 21, 133–140.
Marco E, Dorn JF, Hsu PH, Jaqaman K, Sorger PK, Danuser G (2013). S. cerevisiae chromosomes biorient via gradual resolution of syntely between S phase and anaphase. Cell 154, 1127–1139.
Mastronarde DN (1997). Dual-axis tomography: an approach with alignment methods that preserve resolution. J Struct Biol 120, 343–352.
Mastronarde DN (2005). Automated electron microscope tomography using robust prediction of specimen movements. J Struct Biol 152, 36–51.
Miller SA, Johnson ML, Stukenberg PT (2008). Kinetochore attachments require an interaction between unstructured tails on microtubules and Ndc80(Hec1). Curr Biol 18, 1785–1791.
O'Toole ET, Winey M, McIntosh JR, Mastronarde DN (2002). Electron tomography of yeast cells. Methods Enzymol 351, 81–95.
Pearson CG, Maddox PS, Salmon ED, Bloom K (2001). Budding yeast chromosome structure and dynamics during mitosis. J Cell Biol 152, 1255–1266.
Pearson CG, Yeh E, Gardner M, Odde D, Salmon ED, Bloom K (2004). Stable kinetochore-microtubule attachment constrains centromere positioning in metaphase. Curr Biol 14, 1962–1967.
Roll-Mecak A (2015). Intrinsically disordered tubulin tails: complex tuners of microtubule functions? Semin Cell Dev Biol 37, 11–19.
Sarangapani KK, Akiyoshi B, Duggan NM, Biggins S, Asbury CL (2013). Phosphoregulation promotes release of kinetochores from dynamic microtubules via multiple mechanisms. Proc Natl Acad Sci USA 110, 7282–7287.
Saunders WS, Hoyt MA (1992). Kinesin-related proteins required for structural integrity of the mitotic spindle. Cell 70, 451–458.
Saunders W, Lengyel V, Hoyt MA (1997). Mitotic spindle function in Saccharomyces cerevisiae requires a balance between different types of kinesin-related motors. Mol Biol Cell 8, 1025–1033.
Shimogawa MM, Graczyk B, Gardner MK, Francis SE, White EA, Ess M, Molk JN, Ruse C, Niessen S, Yates JR, *et al.* (2006). Mps1 phosphorylation of Dam1 couples kinetochores to microtubule plus ends at metaphase. Curr Biol 16, 1489–1501.
Spencer F, Gerring SL, Connelly C, Hieter P (1990). Mitotic chromosome transmission fidelity mutants in Saccharomyces cerevisiae. Genetics 124, 237–249.
Stephens AD, Haase J, Vicci L, Taylor RM, Bloom K (2011). Cohesin, condensin, and the intramolecular centromere loop together generate the mitotic chromatin spring. J Cell Biol 193, 1167–1180.
Stephens AD, Haggerty RA, Vasquez PA, Vicci L, Snider CE, Shi F, Quammen C, Mullins C, Haase J, Taylor RM, *et al.* (2013). Pericentric chromatin loops function as a nonlinear spring in mitotic force balance. J Cell Biol 200, 757–772.
Sundin LJ, Guimaraes GJ, Deluca JG (2011). The NDC80 complex proteins Nuf2 and Hec1 make distinct contributions to kinetochore-microtubule attachment in mitosis. Mol Biol Cell 22, 759–768.
Tauchman EC, Boehm FJ, DeLuca JG (2015). Stable kinetochore-microtubule attachment is sufficient to silence the spindle assembly checkpoint in human cells. Nat Commun 6, 10036.
Thomsen MC, Nielsen M (2012). Seq2Logo: a method for construction and visualization of amino acid binding motifs and sequence profiles including sequence weighting, pseudo counts and two-sided representation of amino acid enrichment and depletion. Nucleic Acids Res 40, W281–W287.
Wei RR, Al-Bassam J, Harrison SC (2007). The Ndc80/HEC1 complex is a contact point for kinetochore-microtubule attachment. Nat Struct Mol Biol 14, 54–59.
Westermann S, Avila-Sakar A, Wang HW, Niederstrasser H, Wong J, Drubin DG, Nogales E, Barnes G (2005). Formation of a dynamic kinetochore-microtubule interface through assembly of the Dam1 ring complex. Mol Cell 17, 277–290.
Wigge PA, Kilmartin JV (2001). The Ndc80p complex from Saccharomyces cerevisiae contains conserved centromere components and has a function in chromosome segregation. J Cell Biol 152, 349–360.
Winey M, Bloom K (2012). Mitotic spindle form and function. Genetics 190, 1197–1224.
Winey M, Mamay CL, O'Toole ET, Mastronarde DN, Giddings THJ, McDonald KL, McIntosh JR (1995). Three-dimensional ultrastructural analysis of the Saccharomyces cerevisiae mitotic spindle. J Cell Biol 129, 1601–1615.
Winey M, O'Toole ET (2001). The spindle cycle in budding yeast. Nat Cell Biol 3, E23–E27.
Zaytsev AV, Mick JE, Maslennikov E, Nikashin B, DeLuca JG, Grishchuk EL (2015). Multisite phosphorylation of the NDC80 complex gradually tunes its microtubule-binding affinity. Mol Biol Cell 26, 1829–1844.